













The Eccentric Cavity, Triple Rings, Two-armed Spirals, and Double Clumps of the MWC 758 Disk

Ruobing Dong^{1,2} , Sheng-yuan Liu², Josh Eisner¹ , Sean Andrews³ , Jeffrey Fung⁴, Zhaohuan Zhu⁵, Eugene Chiang⁴ , Jun Hashimoto⁶, Haiyu Baobab Liu⁷, Simon Casassus⁸ , Thomas Esposito⁴ , Yasuhiro Hasegawa⁹, Takayuki Muto¹⁰, Yaroslav Pavlyuchenkov¹¹, David Wilner³ , Eiji Akiyama¹² , Motohide Tamura^{6,13} , and John Wisniewski¹⁴ 

¹ Steward Observatory, University of Arizona, Tucson, AZ 85721, USA

² Institute of Astronomy and Astrophysics, Academia Sinica, Taipei 10617, Taiwan

³ Harvard-Smithsonian Center for Astrophysics, 60 Garden Street, Cambridge, MA 02138, USA

⁴ Department of Astronomy, University of California at Berkeley, Campbell Hall, Berkeley, CA 94720-3411, USA

⁵ Department of Physics and Astronomy, University of Nevada, Las Vegas, 4505 South Maryland Parkway, Las Vegas, NV 89154, USA

⁶ Astrobiology Center of NINS, 2-21-1, Osawa, Mitaka, Tokyo 181-8588, Japan

⁷ European Southern Observatory (ESO), Karl-Schwarzschild-Str. 2, D-85748 Garching, Germany

⁸ Departamento de Astronomia, Universidad de Chile, Casilla 36-D, Santiago, Chile

⁹ Jet Propulsion Laboratory, California Institute of Technology, Pasadena, CA 91109, USA

¹⁰ Division of Liberal Arts, Kogakuin University, 1-24-2 Nishi-Shinjuku, Shinjuku-ku, Tokyo 163-8677, Japan

¹¹ Institute of Astronomy, Russian Academy of Sciences, Moscow, Russia

¹² National Astronomical Observatory of Japan, 2-21-1 Osawa, Mitaka, Tokyo 181-8588, Japan

¹³ Department of Astronomy, The University of Tokyo, 7-3-1, Hongo, Bunkyo-ku, Tokyo 113-0033, Japan

¹⁴ H. L. Dodge Department of Physics & Astronomy, University of Oklahoma, 440 W. Brooks St., Norman, OK 73019, USA

Received 2018 March 26; revised 2018 May 17; accepted 2018 May 18; published 2018 June 20

Abstract

Spatially resolved structures in protoplanetary disks hint at unseen planets. Previous imaging observations of the transitional disk around MWC 758 revealed an inner cavity, a ring-like outer disk, emission clumps, and spiral arms, all possibly generated by companions. We present ALMA dust continuum observations of MWC 758 at 0.87 mm wavelength with 43×39 mas angular resolution (6.9×6.2 au) and $20 \mu\text{Jy beam}^{-1}$ rms. The central submillimeter emission cavity is revealed to be eccentric; once deprojected, its outer edge can be well fitted by an ellipse with an eccentricity of 0.1 and one focus on the star. The broad ring-like outer disk is resolved into three narrow rings with two gaps in between. The outer two rings tentatively show the same eccentricity and orientation as the innermost ring bounding the inner cavity. The two previously known dust emission clumps are resolved in both the radial and azimuthal directions, with radial widths equal to $\sim 4 \times$ the local scale height. Only one of the two spiral arms previously imaged in near-infrared (NIR) scattered light is revealed in ALMA dust emission, at a slightly larger stellocentric distance owing to projection effects. We also submit evidence of disk truncation at ~ 100 au based on comparing NIR imaging observations with models. The spirals, the north clump, and the truncated disk edge are all broadly consistent with the presence of one companion exterior to the spirals at roughly 100 au.

Key words: planet–disk interactions – planets and satellites: formation – protoplanetary disks – stars: individual (MWC 758) – stars: variables: T Tauri, Herbig Ae/Be

Supporting material: tar.gz file

1. Introduction

Planets form in protoplanetary disks surrounding newborn stars typically 1 to a few million yr old. Forming planets perturb the disks via gravitational interactions and may produce large-scale structures such as spiral density waves and gaps (e.g., Goldreich & Tremaine 1980; Lin & Papaloizou 1993; Bryden et al. 1999). Such structures may have been detected in optical to near-infrared (NIR) scattered-light imaging (e.g., spirals: Muto et al. 2012; Stolker et al. 2017; Uyama et al. 2018; Canovas et al. 2018; gaps: Debes et al. 2013; Pinilla et al. 2015; Pohl et al. 2017) and (sub)millimeter to centimeter interferometric observations of disks (e.g., spirals: Pérez et al. 2016; gaps: Canovas et al. 2015; Isella et al. 2016; Dong et al. 2017b; Dipierro et al. 2018). Disk gaps, spiral arms,

and other structures may help infer the presence of (unseen) planets forming in disks and constrain fundamental parameters of these planets, such as mass, location, and orbit.

Here we target a young star+disk system, MWC 758, with previously imaged structures suggestive of carving by planetary-mass companions. MWC 758 is a 3.5 ± 2 Myr (Meeus et al. 2012) Herbig Ae star located at a distance of 160 ± 2 pc (Gaia Collaboration et al. 2018). It is surrounded by a protoplanetary disk in Keplerian rotation (Isella et al. 2010). The disk has a large cavity of ~ 50 au in radius in submillimeter continuum emission (Andrews et al. 2011). It also has a set of near-symmetric two-arm spirals at ~ 30 – 75 au in NIR scattered light (Grady et al. 2013; Benisty et al. 2015) and two emission clumps at tens of au in submillimeter to centimeter continuum emission (Marino et al. 2015; Casassus et al. 2018). Boehler et al. (2018) presented ALMA Cycle 3 observations of MWC 758 in both 0.88 mm continuum emission and $^{13}\text{CO}/\text{C}^{18}\text{O}$ $J = 3$ – 2 emission with $0''1$ – $0''2$ angular resolution. The known \sim millimeter dust ring was



Original content from this work may be used under the terms of the [Creative Commons Attribution 3.0 licence](https://creativecommons.org/licenses/by/3.0/). Any further distribution of this work must maintain attribution to the author(s) and the title of the work, journal citation and DOI.

resolved into a double ring, and a compact emission source centered on the star was identified. The spiral arms were seen in ^{13}CO emission.

Generally speaking, cavities, spiral arms, and emission clumps may reflect gaps, density waves, and vortices dynamically induced by disk-embedded planets (e.g., Zhu et al. 2011; Lyra & Lin 2013; Zhu & Stone 2014; Bae et al. 2016; Hammer et al. 2017). Specifically, Dong et al. (2015b) showed that the MWC 758 disk’s two arms can be quantitatively explained as the primary and secondary spiral shocks driven by one multi- M_J mass companion exterior to the arms. Very recently, Ren et al. (2018) measured the pattern speed of the arms using multi-epoch scattered-light observations and concluded that the best-fit pattern speed corresponds to the Keplerian speed at $r \sim 90$ au from the star. This is consistent with the hypothesis that they are excited by a companion at that radius.

In this paper, we present ALMA Cycle 5 continuum emission observations of the MWC 758 disk at 0.87 mm with an angular resolution of 43×39 mas (6.8×6.2 au), comparable to the angular resolution in NIR direct imaging ($0''.04$ at the H band) and roughly four times better than the highest angular resolution achieved in previous \sim millimeter observations of this target. Nearly all major known disk features are confirmed and further resolved. The main new discoveries include the ellipticity of the central cavity, a triple-ring structure most noticeable toward the west, and the submillimeter continuum emission counterpart of the southern spiral arm imaged in scattered light. In addition, both emission clumps are now resolved in the radial direction for the first time.

2. ALMA Observations and Calibration

Our observations, including three execution blocks (EBs) toward MWC 758, were carried out in Cycle 5 by ALMA under project 2017.1.00492.S. The first EB was conducted on 2017 November 12 with 48 antennas in the array configuration C43-8. The other two EBs were conducted on 2017 November 25 with 48 and 49 antennas in the same C43-8 array configuration. The combined data set has baselines ranging between 92 m and 11.84 km, which correspond to angular scales between $\sim 1''.8$ and $0''.009$. The total integration time on source is about 125 minutes. Typical precipitable water vapor during the on-source period ranges between 0.55 and 0.8 mm.

Four spectral windows centered at 336.495, 338.432, 348.495, and 350.495 GHz, each with an effective bandwidth of 1.78125 GHz and 128 spectral channels under the time division mode (TDM), were employed to maximize the continuum sensitivity. During all three executions, J0510+1800 served as the pointing, bandpass, amplitude, and check calibrator, while J0521+2112 was used as the phase calibrator. The flux scale was calibrated against J0510+1800, which has a spectral index of -0.375 and fluxes set as 1.331, 1.445, and 1.445 Jy at 348.495 GHz for the three EBs, respectively.

Data were first processed and calibrated through the ALMA pipeline calibration procedures under the Common Astronomy Software Applications (McMullin et al. 2007). Imaging of the continuum emission is subsequently achieved by using all four TDM spectral windows with potential spectral contamination inspected. We used the Briggs weighting scheme with a robust parameter of 0.5 and an additional uv tapering (uvtaper parameter = [80000k λ , 4500k λ , -1°] in the tclean task) for

forming a relatively circular beam and improving the signal-to-noise ratio. This results in a synthesized beam size of 43×39 mas (6.8×6.2 au) at PA = -4.3° and an rms noise level of $20 \mu\text{Jy beam}^{-1}$. The continuum emission is detected with a peak signal-to-noise ratio (S/N) of 80. The reduced data cube is available as online supplemental material. Another version of the image synthesized using the natural weighting scheme (not shown in the paper) can also be found in the online supplemental material.

3. Main Features

Figure 1 shows the synthesized image of the continuum emission from MWC 758 at 343.5 GHz (0.87 mm). The disk is detected at $\geq 3\sigma$ out to $\sim 0''.64$ (102 au; see the 3σ contour in panel (b)). This high-resolution map reveals rich features, including a central cavity, a broad outer disk composed of three narrow rings (inner, middle, and outer ring) and two narrow gaps in between, a north clump at the outer edge of the disk, a south clump at the outer edge of the cavity, a central point source, and a spiral arm in the south. Table 1 lists the location, size, and flux measurements of some of the features. The total flux density integrated over a circle of a diameter of $1''.3$ in size encompassing the disk extent is 180 mJy, comparable to the values of 180 mJy at 340 GHz measured with the Submillimeter Array by Andrews et al. (2011) and 205 mJy at 337 GHz with ALMA by Marino et al. (2015). The differences at the $\sim 10\%$ level may arise from flux calibration uncertainties or missing short uv sampling. In the latter case, the missing flux would correspond to a smooth and low surface brightness structure roughly $\sim 30 \mu\text{Jy beam}^{-1}$ or 1.5σ in brightness. The resulting effects in the measurements of amplitude peaks and contrasts are small.

3.1. The Central Point Source and the Nondetection of Circumplanetary Disks

The central point source (inset, Figure 1(b)) is detected at the 9σ level with a peak flux of $0.17 \text{ mJy beam}^{-1}$. The resolution constrains the point-source size to be < 3 au in radius. Given the incomplete short spacing coverage, there is a residual negative bowl within the central cavity at a $0.04 \text{ mJy beam}^{-1}$ level ($\sim 2\sigma$). When fitted with a circular Gaussian with noises and the negative floor inside the cavity factored in, the actual integrated flux density of the central source is around 0.18 mJy. As in Boehler et al. (2018), in which the point source was also detected around the location of the star, we assume it originates from a small circumstellar structure previously detected in infrared interferometric observations (Eisner et al. 2004). A 2 yr baseline established by the Boehler et al. (2018) observations and our observations rules out the source being a background (nonmoving) object based on MWC 758’s proper motion (27 mas yr^{-1} ; Gaia Collaboration et al. 2018). Combining with the total flux density of the central source measured at $\nu = 33$ GHz by the VLA ($F(33 \text{ GHz}) = 67 \mu\text{Jy}$; Marino et al. 2015), we derive a spectral index $\alpha = \log((F(\nu_1)/F(\nu_2))/\log(\nu_1/\nu_2)) = 0.4$ between 343.5 and 33 GHz, consistent with the α derived between 33 and 15 GHz (0.36; Marino et al. 2015). This value is significantly flatter than $\alpha = 2$, expected if the source is optically thick, or $\alpha = 2 + \beta$, where β is the dust opacity index (usually a positive number; Draine 2006), expected if the source is optically thin. Such a low value indicates the contribution (or dominance) of free-free emission from ionized gas (e.g., the disk wind) very

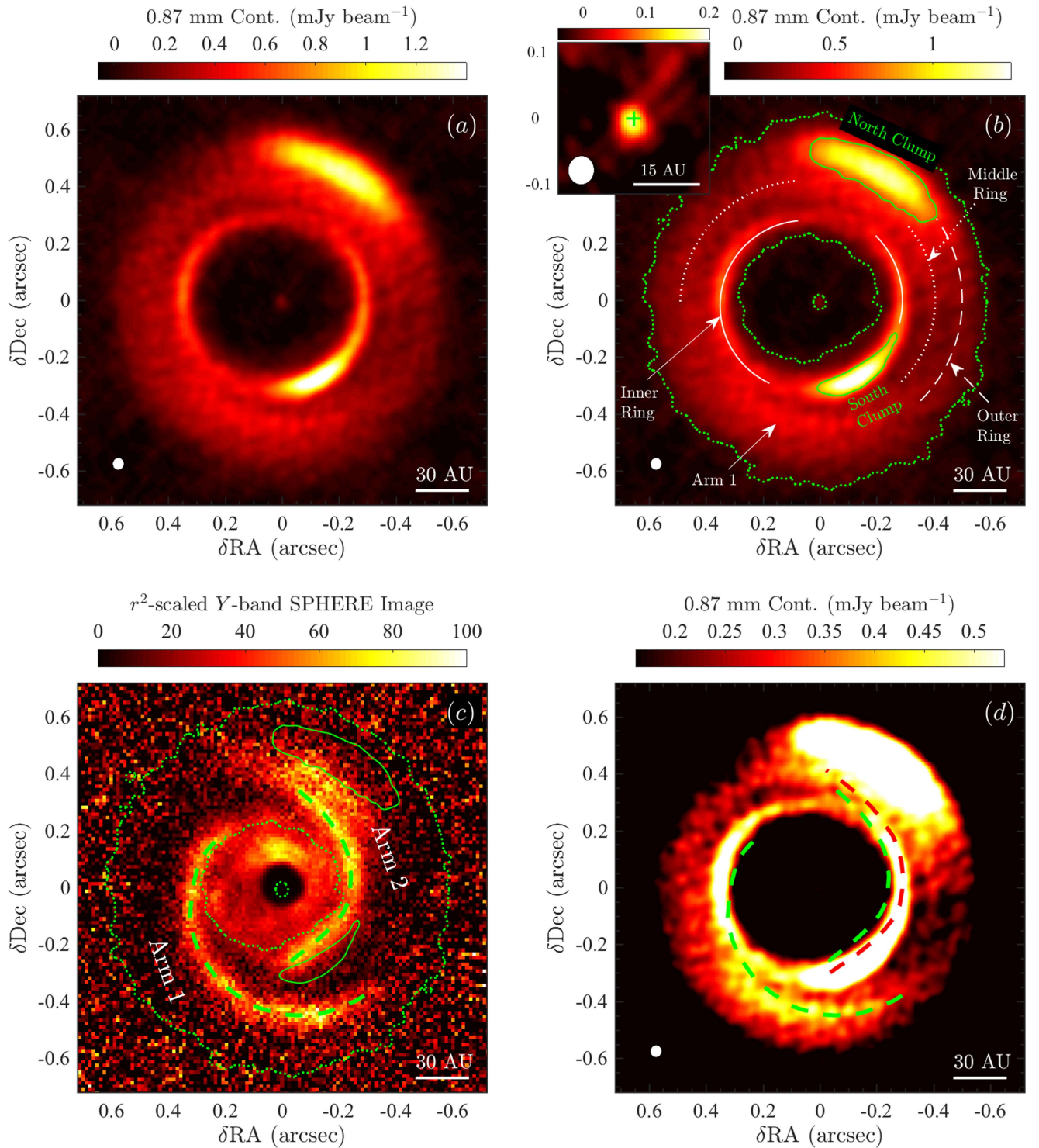


Figure 1. Panels (a) and (b): ALMA 0.87 mm continuum emission from MWC 758 with a beam size 43×39 mas (6.9×6.2 au; labeled at the lower left corner). North is up and east is to the left. In panel (b), the structures are labeled: the green dotted contours are at the 3σ noise level; the two green solid contours are at half-peak intensity at each clump; the solid, dotted, and dashed white arcs trace the inner, middle, and outer rings, respectively; and the inset is a $0''.2$ zoom of the central region (stellar location marked by the green plus). Panel (c) shows an r^2 -scaled SPHERE Y-band ($1 \mu\text{m}$) polarized scattered-light image (Benisty et al. 2015; normalized unit). The contours in panel (b) are overlaid, and the two green dashed lines trace the locus of the two spiral arms (labeled as Arm 1 and Arm 2; the two green curves are overlaid in panel (d) as well). The astrometrical alignment between the SPHERE and ALMA images is done by aligning the location of the central star. The absolute stellar position in the SPHERE image may be accurate to half the SPHERE pixel size (6 mas). Panel (d) shows the emission map with an aggressive color stretch to highlight ALMA Arm 1. The red dashed curve is the locus of SPHERE Arm 2 shifted away from the star by $0''.05$. The south part of SPHERE Arm 1 is revealed at a slightly larger stellocentric distance by ALMA. Arm 2 cannot be clearly identified in the continuum emission. The FITS file for panel (a) is available as online supplemental material.

close to the star (e.g., Liu et al. 2017). Alternatively, it may indicate self-absorbed dust emission in the dense \sim au-scale circumstellar region (Li et al. 2017).

We note that the fitted Gaussian position of this source is offset by ~ 7 mas to the south-southeast from the Gaia Collaboration et al. (2018; the proper motion of the star has

Table 1
Feature Properties and Their 1σ Uncertainties Measured in the Deprojected ALMA 0.87 mm Continuum Emission Map (Figure 2)

Feature	Radius	PA	FWHM	FWHM	I_{peak}	$T_{\text{B,peak}}$	$I_{\text{peak}}/I_{\text{trough}}$
(1)	(2)	(3)	Radial	Azimuthal	mJy beam ⁻¹	K	(8)
			(4)	(5)	(6)	(7)	
Arm 1	$0''.453 \pm 0''.006$	$175^\circ \pm 1^\circ$	0.51 ± 0.02	9.0 ± 0.2	3.6 ± 0.5
South clump	$0''.306 \pm 0''.003$	$206^\circ \pm 2^\circ$	$0''.075 \pm 0''.001$	$56^\circ \pm 1^\circ$	1.60 ± 0.02	16.8 ± 0.1	4.4 ± 0.3
North clump	$0''.533 \pm 0''.006$	$335^\circ \pm 1^\circ$	$0''.160 \pm 0''.003$	$54^\circ \pm 1^\circ$	1.28 ± 0.02	14.7 ± 0.1	10 ± 1
Inner ring	$0''.319 \pm 0''.002$...	$0''.085 \pm 0''.005$...	0.70 ± 0.02	10.5 ± 0.2	...
Middle ring	$\sim 0''.43$	0.32 ± 0.02	7.4 ± 0.2	...
Outer ring	$\sim 0''.54$	0.29 ± 0.02	7.1 ± 0.2	...

Note. Only quantities that can be robustly measured are listed. Column (1): name of the feature (labeled in Figure 1(b)). Column (2): stellocentric radius at the peak. For the inner ring, it is the semimajor axis in the ellipse fit in Section 3.2 (see also Figure 2(c)); for the middle and outer rings, it is the semimajor axis in the tentative ellipse fits (these two rings are very incomplete). Column (3): position angle at the peak. Column (4): full width at half maximum in the radial direction. For the two clumps, the measurement is done at the peak PA listed in column (3). For the inner ring, it is the average FWHM measured in the “ring west” ($0''.08$) and “ring east” regions ($0''.09$) in Figure 2(c). The middle and outer rings do not permit such a measurement. Column (5): full width at half maximum in the azimuthal direction for the two clumps measured at the peak radius listed in column (2). Column (6): peak intensity (surface brightness). For the inner ring, it is the peak intensity on the east side, as the west side may contain contributions from the south clump. For the middle and outer rings, it is the peak azimuthally averaged intensity in the “ring west” region in Figure 2(c). Column (7): brightness temperature corresponding to the peak intensity in column (6), converted using the Planck function. Column (8): azimuthal peak-to-trough intensity ratio. For the north clump and the spiral, the trough intensity is taken as the minimum intensity along the circle at the radius listed in column (2). For the south clump, the trough intensity is taken as the minimum intensity along the elliptical inner ring.

been accounted for) stellar location (same as the phase center). This may be due to astrometry errors in phase referencing or position uncertainties from phase noise. The astrometry error based on the check source J0510+1800 is, on average, 2 mas. The position uncertainty due to phase noise is at a level of 2 mas, given the signal-to-noise ratio and the beam size (i.e., $0.45 \times \text{beam size}/(S/N)$; Reid et al. 1988; Wright et al. 1990). There remains the possibility of a true sub-au-scale asymmetry in the inner disk to be examined in the future.

Other than the central source, we do not detect any compact point source at the 3σ level that may be associated with circumplanetary disks (CPDs) around forming planets. Hydro simulations have shown that the radius of a circum-companion disk is $\sim 1/3$ of the companion’s Hill radius (Martin & Lubow 2011). At $r \leq 100$ au, the diameter of such a disk is smaller than 10 au, or twice the beam size of our ALMA observation, for any object with $M_p \leq 13M_J$. Considering that submillimeter continuum emission from such a disk is probably centrally peaked and compact (e.g., Wu et al. 2017), we do not expect to significantly resolve such a disk at $r \leq 100$ au if detected (see also simulated ALMA images of CPDs in Szulágyi et al. 2017). Inside the cavity and outside the 3σ contour at $r \sim 0''.64$ in Figure 1(b), where the emission reaches the noise floor, the 3σ upper limit on the flux density of unresolved point sources is $60 \mu\text{Jy}$. Within the broad outer disk, the detection limit is higher due to background disk emission.

3.2. The Cavity and the Outer Disk

The cavity and the narrow inner ring at the cavity edge in Figure 1(a) appear to be noncircular and off-center. This is not a projection effect. Figure 2 shows the deprojected view of the disk in Cartesian and polar (radial-azimuthal) coordinates assuming an inclination $i = 21^\circ$ and position angle $\text{PA} = 62^\circ$ (Isella et al. 2010; Boehler et al. 2018); the origin of the polar coordinate system is set to be at the expected *Gaia* stellar location. We note that the inclination and PA correspond to the outer disk outside the cavity. The system may have a mildly warped (misaligned) inner gas disk inside $\sim 0''.1$, with an inclination in the range of 30° – 40° (Eisner et al. 2004; Isella et al. 2008; Boehler et al. 2018). Since \sim millimeter-sized dust

traced by ALMA continuum emission is expected to settle to a thin layer at the disk midplane (e.g., Dullemond & Dominik 2004), deprojection roughly recovers the face-on view of the disk. The noncircular and off-center cavity is clearly evident in deprojected maps—circles centered on the star would be horizontal straight lines under the polar view. The deprojected inner ring is well approximated by an ellipse with one focus on the star (note that the central point source roughly coincides with the *Gaia* stellar location, which is set to be the phase center), semimajor axis $a = 0''.319 \pm 0.002$, eccentricity $e = 0.10 \pm 0.01$, and major axis $\text{PA} = 95^\circ \pm 10^\circ$.

Our conclusion that the cavity is not a circle is derived primarily from the inferred offset of the center of the ring from the stellar position. The deprojected inner ring may also be approximated by a circle with a radius $r = 0''.320 \pm 0''.003$. However, its center is at $(\delta\text{R.A.}, \delta\text{decl.}) = (33 \pm 2 \text{ mas}, -5 \pm 3 \text{ mas})$ from the expected (*Gaia*) stellar position. This difference is \sim one order of magnitude larger than the expected ALMA astrometry uncertainty (Section 3.1 and Section A.9.5 in the ALMA Cycle 6 Proposal Guide). It is therefore very unlikely for the expected stellar location to offset from its actual location by ~ 30 mas. In addition, the detection of the central submillimeter point source at roughly the expected stellar location suggests that it is within a few mas from the actual stellar location, as the point source is likely a small circumstellar disk. We also find no good physical motivation and consider it very unlikely for the cavity to be a true circle but significantly off-centered. Future simultaneous high-resolution observations of both the gas and the dust emission may provide more definitive evidence on the eccentric cavity.

Two depressions on the inner ring can be identified around $\text{PA} \sim 0^\circ$ and 135° , between which are two bright arcs on the west and east sides. The “Ring East” and “Ring West” regions defined in Figure 2(c) are relatively free from “contaminations” from other features. We use them to study the radial structures (rings and gaps) in the outer disk at $r \sim 0''.25$ – $0''.60$.

Figure 3(a) plots the azimuthally averaged radial profiles in these two regions. The Ring East region shows a global peak corresponding to the inner ring and a second peak at $0''.45$. The Ring West region shows the same inner ring at a smaller radius due to its eccentric nature and two peaks in the outer disk at

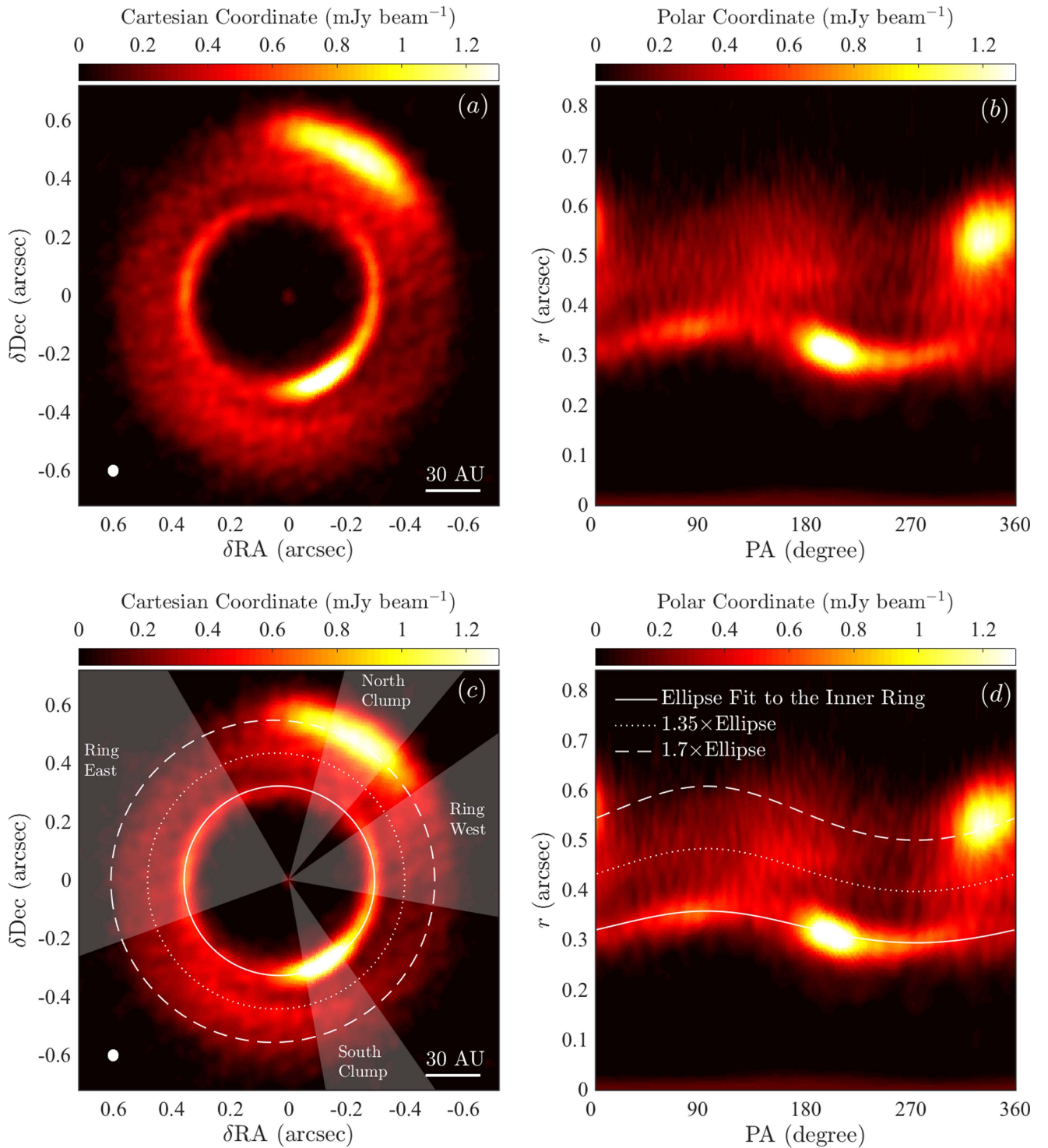


Figure 2. Deprojected image of MWC 758 assuming $i = 21^\circ$ and $PA = 62^\circ$ in Cartesian and polar (radial-azimuthal) coordinates. The top and bottom rows are identical, apart from the annotations. In panel (c), the three curves are three ellipses, $1\times$, $1.35\times$, and $1.7\times$ the size of the ellipse fit to the inner ring at the cavity edge ($a = 0''.32$, $e = 0.1$, and one focus on the star), and the four shaded regions are the selected azimuthal directions (their radial profiles are plotted in Figures 3(a) and (c)). In panel (d), the three curves are the three ellipses in panel (c) (line types are consistent). They roughly trace (inside to outside) the inner ring and the visible portion of the middle and outer rings marked in Figure 1(b). The cavity is off-center and noncircular. See Sections 3.2 and 4.1 for discussion.

$0''.40$ and $0''.51$. We cannot trace the 2π extent of these outer rings, as the emission is segmented into a west and an east part by the north clump and the region around Arm 1. Nevertheless, we tentatively associate the $0''.45$ peak on the Ring East and the $0''.40$ peak on the Ring West profile with a common faint middle ring (labeled in Figures 3(a) and 1(b)). The dotted curve in Figure 2(c) is an ellipse with the same orientation and

eccentricity but $1.35\times$ the size of the ellipse fit to the inner ring. It roughly traces and connects the east ($PA \sim 220^\circ\text{--}310^\circ$) and west ($PA \sim 10^\circ\text{--}120^\circ$) segments of the middle ring (we suggest viewing this panel together with the annotation-free version of the polar map and also viewing the ring in Figure 1(d) with a more dramatic color stretch). Similarly, the dashed curve is an ellipse $1.7\times$ bigger; on the west side, it

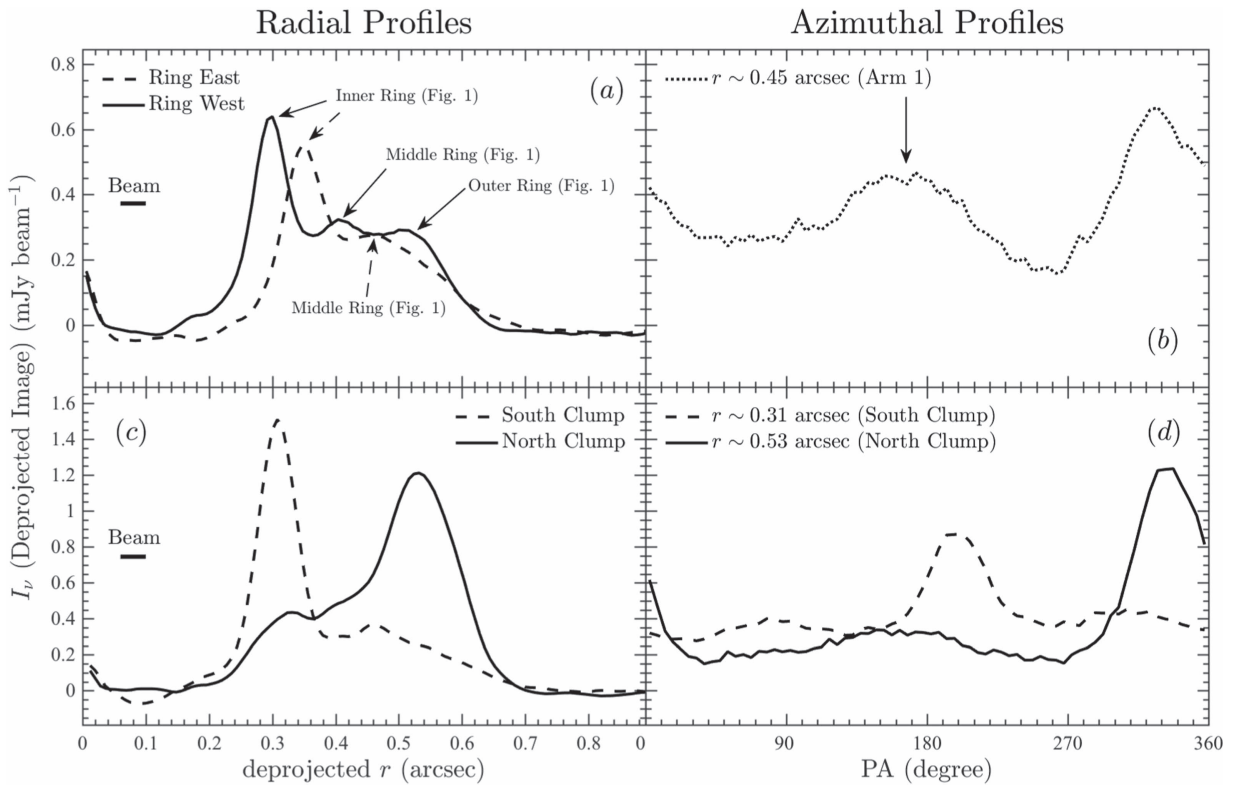


Figure 3. Azimuthally averaged radial profiles in four selected regions (panels (a) and (c)) and radially averaged azimuthal profiles in three circular rings (panels (b) and (d)); the radial widths of the rings are $0''.03$ (Arm 1), $0''.04$ (north clump), and $0''.13$ (south clump) in the deprojected ALMA image (Figure 2). The four regions in panels (a) and (c) are defined as the shaded regions in Figure 2(c), and the three rings in panels (b) and (d) are centered on the peak radii of Arm 1 and the two clumps. See Sections 3.2 and 4.1 for discussions.

roughly traces the faint outer ring (labeled in Figures 3(a) and 1(b)), while on the east side, it passes through a region with a S/N too low to enable robust structure identifications. These two rings merge into the north clump in the north end and touch the spiral region in the south. Both are unresolved in the radial direction; thus, their physical widths are smaller than the beam size (~ 6.5 au). The “outer ring” in the “double-ring” structure detected in a previous ALMA data set (Boehler et al. 2018) with $0''.1$ – $0''.2$ angular resolution may contain both the middle and outer rings in this data set. All three rings (inner, middle, and outer) may share similar eccentricities and orientations, although this needs to be confirmed by future observations.

3.3. The Spirals

MWC 758 has two prominent spiral arms in NIR scattered light (Arm 1 on the east and Arm 2 on the west, labeled in Figure 1(c)). Figure 1(d) shows the map with an aggressive color stretch to highlight the spiral arms. Arm 1 is clearly detected at $r \sim 0''.4$ – $0''.5$ and $\text{PA} \sim 120^\circ$ – 210° . It is resolved in the azimuthal but not the radial direction, setting an upper limit on the physical radial-width-to-radius ratio to be 10%. The east end of the arm starts at the inner ring. The arm weakens and merges into the background at the west end. The peak surface brightness on the arm is $0.51 \text{ mJy beam}^{-1}$ ($\text{S/N} = 25$), reached at ~ 72 au (deprojected; $0''.45$), corresponding to a brightness temperature $T_B = 9.0$ K. The azimuthal peak-to-trough contrast of the spiral in the deprojected image measured along the $r = 0''.45$ circle (no radial or azimuthal averaging) is 3.6. Figure 3(b) shows the azimuthal profile of the deprojected surface brightness averaged over a ring with a radius of $0''.45$ and width of $0''.03$. Arm 2 is not

clearly detected. However, it is possible that part of that arm is present and spatially overlapping with other features (see Section 4.2.2).

3.4. The Double Emission Clumps

The two emission clumps are resolved in both the azimuthal and the radial directions (see the beam size and half-peak contours around the clumps in Figure 1(b)). Figure 3(c) shows the radial profiles across the two clumps. The radial full widths at half maximum (FWHMs) of the south and north clumps in the deprojected image are ~ 1.8 and ~ 3.9 times the beam size, respectively, and the azimuthal FWHM of both clumps is $\sim 1/6$ of a circle. We estimate their intrinsic (deconvolved) radial FWHM ($\text{FWHM}_{\text{intrinsic}} \approx \sqrt{\text{FWHM}^2 - \text{FWHM}_{\text{beam}}^2}$) to be $0''.063$ and $0''.155$ for the south and north clumps, respectively. Figure 3(d) shows the azimuthal profiles of the clumps in the deprojected map. The azimuthal peak-to-trough contrasts of the south and north clumps are 4.4 and 10 at the radii of their peaks, respectively. The peak surface brightnesses in the south and north clumps are 1.60 and $1.28 \text{ mJy beam}^{-1}$, corresponding to $T_B = 16.8$ and 14.7 K, respectively.

We generate representative disk models using the radiative transfer code HOCHUNK3D (Whitney et al. 2013) to obtain crude estimates of the dust temperature T_{dust} at these radii. The models largely follow the radiative transfer model for MWC 758 presented in Grady et al. (2013). They assume a full disk with surface density $\Sigma \propto 1/r$, as the μm -sized dust probed by scattered light is present inside the cavity (Benisty et al. 2015; the starlight is mainly absorbed and scattered by the small dust). The central star is assumed to have $T_* = 7580$ K and $L_* = 9.7 L_\odot$ after

scaling the stellar luminosity in Andrews et al. (2011) by the new *Gaia* distance. With a variety of disk scale heights ($h = 5\text{--}20$ au at $r = 100$ au) and disk flaring angles ($h/r \propto r^{0.05}$ to $h/r \propto r^{0.25}$), we obtain $T_{\text{dust}} = 20\text{--}32$ K at the location of the south clump (deprojected $r = 0''.31 = 50$ au) and $17\text{--}27$ K at the location of the north clump (deprojected $r = 0''.53 = 85$ au). The two clumps may be marginally optically thin (vertical optical depth of order unity). The same models also yield $T_{\text{dust}} = 18\text{--}27$ at the location of Arm 1 ($r \sim 70$ au after deprojection), significantly higher than the T_{B} (9.0 K).

4. Discussion

4.1. The Eccentric Cavity and Rings

Rings with eccentricities $e \gtrsim 0.1$ have been found or inferred in debris disks (Kalas et al. 2005; Lee & Chiang 2016). To our knowledge, MWC 758 as revealed in our ALMA data set provides the first known example of an intrinsically eccentric protoplanetary disk.

One hypothesis for the origin of transitional disks is that their cavities are opened by (multiple) companions, possibly planets. Simulations have shown that the outer edge of a gap opened by a companion on a circular orbit may become eccentric (e.g., Kley & Dirksen 2006; Dunhill et al. 2013; Farris et al. 2014; Teyssandier & Ogilvie 2017). The gap edge eccentricity is excited by interactions between the companion and the disk at the outer 1:3 Lindblad resonance (LR; the eccentric instability, Lubow 1991a, 1991b) and damped by the 1:2 LR and the co-orbital resonance; therefore, a gap wide enough to extend past the outer 1:2 but not the 1:3 LR may develop a nonzero eccentricity (Kley & Dirksen 2006). A higher companion mass, lower disk viscosity, and lower disk temperature facilitate the opening of deep and wide gaps (Fung et al. 2014), and thus the growth of e . In this scenario, the outermost planet inside the cavity should be located between 0.48 and 0.63 of the cavity outer edge in the gas, or 25–32 au, assuming that $r_{\text{gas,cavity}} = r_{\text{dust,cavity}} = 0''.32 = 51$ au. Since the cavity size in the gas is expected to be smaller than it is in dust emission due to gas–dust coupling at the gas cavity edge (Pinilla et al. 2012; Zhu et al. 2012), the planet may be at a smaller stellocentric radius.

The eccentric cavity and outer disk precess at a frequency much lower than the local Keplerian frequency Ω_{K} (e.g., Teyssandier & Ogilvie 2017). Hsieh & Gu (2012) showed that in this case, the eccentric outer disk does not trap \sim millimeter-sized particles in the azimuthal direction. Thus, we do not expect the two observed emission clumps to be global dust traps produced by the eccentric disk. Instead, they may be generated by other mechanisms, such as dust trapping by vortices (see Section 4.3). An eccentric gap may coexist with vortices in disk–planet interaction models (Ataiee et al. 2013).

Eccentric cavities and rings can alternatively be opened by companions on eccentric orbits. We note that giant planets with masses of several M_{J} interacting with a gaseous disk may grow their eccentricities to ~ 0.1 , comparable to the eccentricity observed here (Dunhill et al. 2013; Duffell & Chiang 2015; Ragusa et al. 2017). In this scenario, the orbits of the cavity-opening and gap-opening planet(s) in MWC 758 may share similar eccentricities and orientations. Future studies are needed to investigate this hypothesis.

4.2. The Spiral Arms

Among the new features, perhaps the most exciting one is the discovery of the submillimeter continuum counterpart to the NIR spiral on the south. Spiral arms in protoplanetary disks have been detected in NIR scattered light (e.g., Fukagawa et al. 2006; Hashimoto et al. 2011; Muto et al. 2012; Canovas et al. 2013, 2018; Garufi et al. 2013; Currie et al. 2014; Wagner et al. 2015; Akiyama et al. 2016b; Liu et al. 2016; Stolker et al. 2016a; Avenhaus et al. 2017; Benisty et al. 2017; Follette et al. 2017; Long et al. 2017; Maire et al. 2017; Langlois et al. 2018) and in \sim millimeter gas (e.g., Corder et al. 2005; Christiaens et al. 2014; Tang et al. 2017) and dust emission (e.g., Pérez et al. 2016; Tobin et al. 2016). A few mechanisms have been explored to explain their origin, including companion–disk interaction (e.g., Dong et al. 2015b; Zhu et al. 2015; Bae et al. 2016), gravitational instability (GI; e.g., Dipierro et al. 2015; Dong et al. 2015a, 2016b; Hall et al. 2016, 2018; Meru et al. 2017; Tomida et al. 2017), a combination of GI + planet (Pohl et al. 2015), finite light travel time (e.g., Kama et al. 2016), and moving shadows (e.g., Montesinos et al. 2016; Montesinos & Cuello 2018). For planet-induced spiral arms, their morphology and brightness can be used to constrain the mass of the perturber (Fung & Dong 2015; Dong & Fung 2017).

Except in rare cases (e.g., HD 100453, in which the spiral arms are driven by a visible stellar-mass companion bound to the system; Dong et al. 2016c; Wagner et al. 2018), the true origin of the observed spiral arms, in particular whether they are planet-induced, is under debate. For MWC 758, the low disk mass (M_{disk} estimated from submillimeter continuum emission ($M_{\text{disk}} \sim 1\% M_{\star}$; Andrews et al. 2011) disfavors the GI scenario, which usually requires $M_{\text{disk}} \gtrsim 10\% M_{\star}$ under typical conditions (Kratler & Lodato 2016). Spatially resolved observations of spirals revealing their shapes, contrasts, and locations at multiwavelengths are crucial to a thorough understanding of their origins.

Companion-induced spiral arms are pressure waves. They only directly manifest in a pressure-supported medium: the gas. Whether they are present in submillimeter continuum emission depends on whether they can trap \sim millimeter-sized dust particles. Such spirals, corotating with their drivers, have a nonzero relative angular velocity with respect to the local disk, different from GI-induced spirals. While the latter are capable of trapping particles of certain sizes (e.g., Rice et al. 2004; Dipierro et al. 2015), whether and how companion-induced spiral arms can trap dust is uncertain. Further, while the primary arm (the one directly pointing to the companion) has been thoroughly studied (e.g., Goldreich & Tremaine 1979; Goodman & Rafikov 2001; Ogilvie & Lubow 2002; Rafikov 2002), the excitation, properties, and propagation of the secondary (and additional) arm driven by a single companion is still ongoing research (e.g., Juhász et al. 2015; Lee 2016; Arzamasskiy & Rafikov 2018; Bae & Zhu 2018a, 2018b; Hord et al. 2017; Juhász & Rosotti 2018).

With the nature of the two arms still uncertain, the large azimuthal peak-to-trough contrast of Arm 1 in the deprojected submillimeter continuum emission suggests that it is mainly a density (emission optical depth) feature. The spiral is unlikely to be a shadow or temperature feature, as no evidence of the shadow is seen in NIR scattered light. If the dust is optically thin and the structure is spatially resolved, the submillimeter emission intensity I_{ν} at a frequency ν is proportional to $\Sigma_{\text{dust}} \times \kappa_{\nu,\text{dust}} \times B_{\nu}(T_{\text{dust}})$, where Σ_{dust} and $\kappa_{\nu,\text{dust}}$ are the surface density and opacity of the

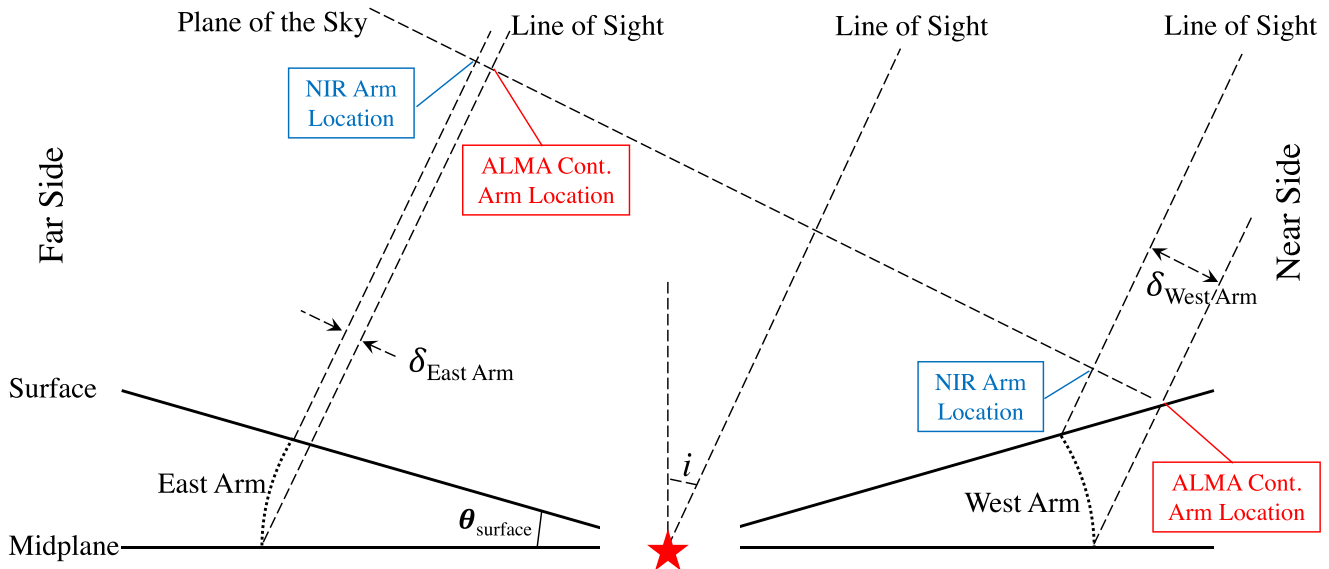


Figure 4. Schematic of ALMA and NIR imaging observations of a disk with two planet-induced spiral arms viewed from the side. The observer is to the northwest. The same spiral arm can be projected to different locations on the plane of the sky in NIR scattered light (probing surface features) and \sim millimeter continuum emission (probing midplane features). The East Arm in NIR scattered light is at a larger distance from the star than it is in ALMA continuum emission, while it is the opposite for the West Arm. This is caused by both the curved vertical structure of the spiral arms (illustrated by the dotted curves) and the inclination of the disk. See Section 4.2 for discussion.

submillimeter continuum-emitting dust, and $B_\nu(T_{\text{dust}})$ is the Planck function at the dust temperature T_{dust} . Note that Arm 1 is not resolved radially in our ALMA observations, and the measured azimuthal contrast is only the lower limit of the “intrinsic” azimuthal contrast in I_ν with infinite angular resolution. If Arm 1 is caused by variations in T_{dust} , as in the shadow scenario (Montesinos et al. 2016; Montesinos & Cuello 2018), at least order unity variation in T_{dust} in the azimuthal direction across the arm is needed, which seems physically unlikely. Instead, the arm is most likely introduced by variations mainly in $\Sigma_{\text{dust}} \times \kappa_{\nu, \text{dust}}$, with a possible minor contribution from T_{dust} (e.g., from spiral shock heating; Rafikov 2016).

4.2.1. Why ALMA Arm 1 Is Offset from NIR Arm 1

At PA $\sim 120^\circ$ – 180° , Arm 1 in the ALMA continuum emission map is at a slightly larger stellocentric distance than in NIR scattered light (Figure 1(d); maximum radial offset $\sim 0''.03$, or 8% of the radius). The ALMA arm crosses the NIR arm at PA $\sim 180^\circ$, and the two roughly overlap at PA $\sim 180^\circ$ – 210° . This is most likely caused by the difference between a midplane feature and a surface feature in a projected view, as illustrated in the schematic in Figure 4 (see also Stolker et al. 2016b). When viewed at a finite inclination i , midplane structures probed by ALMA continuum observations are simply compressed by $1/\cos i$ along the direction of the minor axis. Such images are “deprojectable.” On the other hand, scattered light comes from a cone-shaped disk surface. Dong et al. (2016a) showed that surface features at a finite inclination can be dramatically distorted from their morphology at face-on, and such distortions cannot be recovered by simple deprojection. When viewed at nonzero i , “NIR/surface spiral” and “ALMA/midplane spiral” are projected to different locations on the plane of the sky. An additional complication is that spiral arms are curved in the vertical direction—they bend over toward the star (Figure 1, Zhu et al. 2015; Figure 2, Lyra et al. 2016; dotted curves in the schematic). In the schematic,

the surface (NIR) East Arm is further from the star than the midplane (ALMA) East Arm on the plane of the sky, while for the West Arm, it is the opposite.

We present a toy model in Figure 5 to visualize the effect. Synthetic ALMA submillimeter continuum and NIR polarized scattered-light images for one disk model are simulated at three viewing angles using 3D hydrodynamics and radiative transfer simulations. The disk model is taken from Model $3M_J$ in Dong et al. (2016a), which has a planet with $M_p = 3 \times 10^{-3} M_\star$ on a circular orbit at $r = 100$ au, driving two main spiral arms interior to its orbit. The outer disk at $r > 100$ au is removed in postprocessing to highlight the spiral arms. In simulating the ALMA images, continuum-emitting dust is assumed to be millimeter in size. While millimeter-sized dust is not included in the gas-only hydro simulation, its surface density is assumed to be linearly proportional to the gas. The total millimeter-sized dust mass is normalized such that the disk is optically thin at submillimeter wavelengths. In the vertical direction, the density distribution of millimeter-sized dust is assumed to be Gaussian, with the aspect ratio h/r , taken to be 10% of the gas, less than 1% everywhere. We emphasize that proper dust–gas coupling (i.e., realistic trapping of \sim millimeter-sized dust by the spiral arms) is not taken into account, and the toy model is only meant to visualize the ALMA–NIR (equivalently, midplane–surface) arm location offset effect.

At $i = 0$ (panel (b)), both the primary and secondary arms are located roughly at the same locations in the ALMA and NIR images.¹⁵ When inclined, on the near side of the disk, the

¹⁵ In principle, even at face-on, we may still expect a small difference, as the arms tend to bend over toward the star in the vertical direction (see the schematic). In practice, this difference may be small. Usually, the disk aspect ratio h/r is smaller than 0.1 at tens of au. Assuming the disk surface is at three scale heights, the opening angle of the surface from the midplane $\theta_{\text{surface}} \lesssim \arcsin(3 \times 0.1) = 17^\circ$, and $\cos 17^\circ = 0.96$. If, in the vertical direction, the arms bend to maintain a constant distance to the star, we expect a $\lesssim 4\%$ midplane–surface arm location difference at $i = 0$, or $\sim 0''.01$ at 60 au at 140 μm .

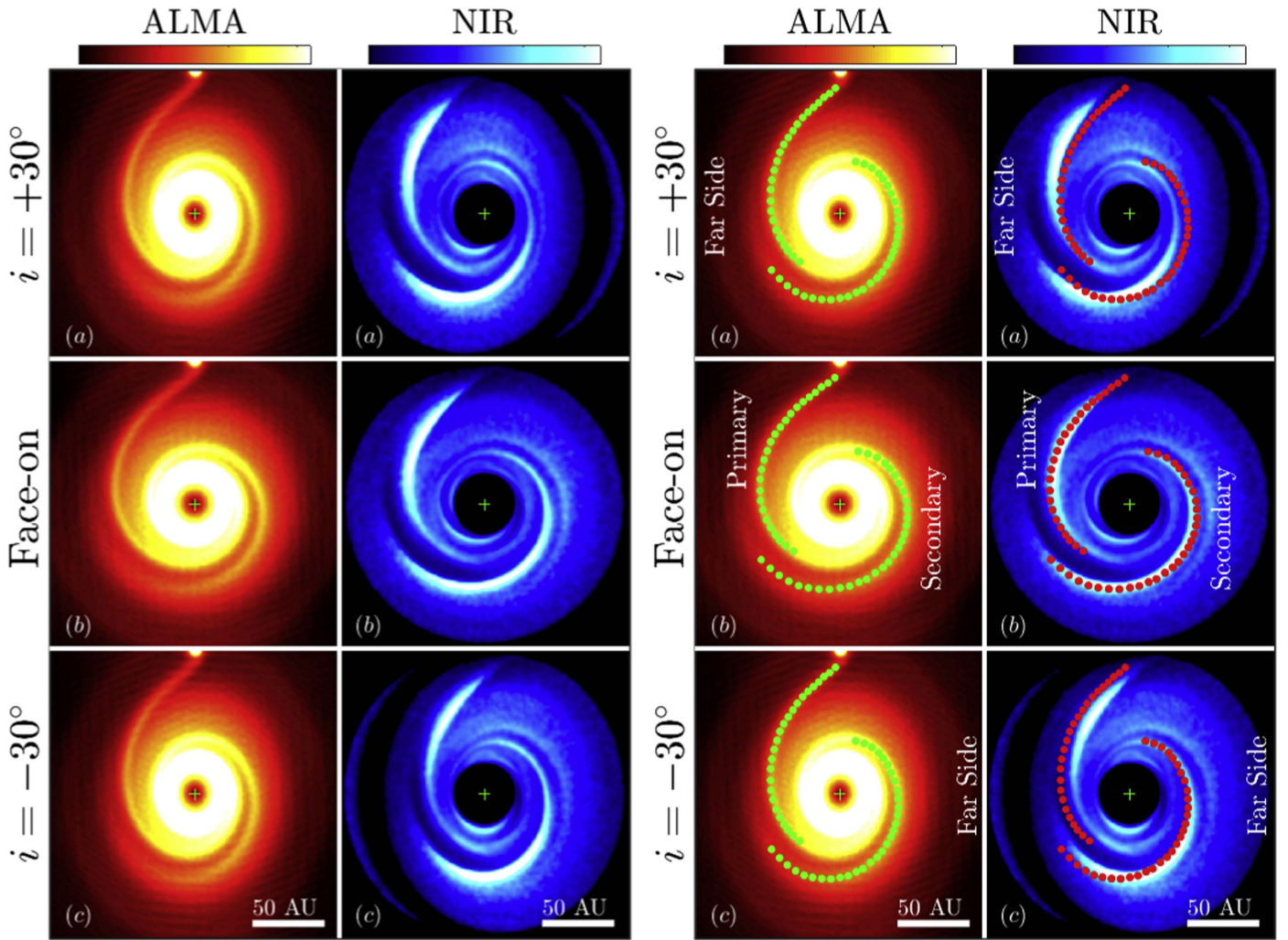


Figure 5. Synthetic ALMA 0.87 mm continuum emission and NIR (H -band) polarized scattered-light images (central part artificially masked) of a toy disk model with two spiral arms excited by a planet ($M_p = 3 \times 10^{-3} M_*$; located at $r = 100$ au and $PA = 0$) at three viewing angles (inclination i labeled on the left and $PA = 0$ in all cases; i.e., the major axis is along north–south), produced using the $3M_J$ model in Dong et al. (2016a). The disk is assumed to be at 151 pc, and images at both wavelengths are convolved to have an angular resolution of $0''.04$. Color stretch is linear, and units are arbitrary. The H -band images have been scaled by r^2 , and ALMA images have been scaled by \sqrt{r} (deprojected r) to highlight the arms. The right half is identical to the left half but with (1) the locus of the two arms in the ALMA image at each viewing angle marked by the dots in both the ALMA and NIR images (the green and red dots are the same), (2) the far side of the disk marked in the top and bottom rows, and (3) the primary and secondary arms labeled in panel (b). The submillimeter continuum-emitting big dust (\sim millimeter-sized) is assumed to have a surface density linearly scaled with the gas and settled to the disk midplane. The locations of the arms in the ALMA continuum observations (midplane features) may differ from where they are in the NIR observations (surface features). See Section 4.2 for discussion.

surface feature moves toward the star faster than the corresponding midplane feature; thus, the NIR arms are found at shorter stellocentric distances than the ALMA arms (the primary in panel (c), the east side of the secondary in panel (c), and the west side of the secondary in panel (a)). On the far side, the NIR arms stay roughly at the same locations, while the ALMA arms approach the star, thus displacing the two (the primary in panel (a), the east side of the secondary in panel (a), and the west side of secondary in panel (c)). Also note that in the NIR images, a weak third arm right outside the secondary is present. This arm is mainly a surface feature caused by varying scale height, not a surface density feature, and is therefore not visible in the ALMA images.

The difference in the arm locations in the NIR and ALMA images (δ in the schematic) depends on (1) i , (2) PA, (3) the opening angle of the scattered-light surface θ_{surface} , and (4) the arm structure in the vertical direction. Once item (4) is thoroughly understood, an accurate measurement of δ

combined with a known disk inclination may constrain θ_{surface} . If multiwavelength scattered-light images (e.g., from the optical to L band) are available, the arms may move slightly across wavelengths as θ_{surface} drops with increasing wavelength. Finally, we note that Boehler et al. (2018) detected Arm 1 in ALMA ^{13}CO emission with a coarse beam ($\sim 0''.2$) and concluded that it coincides with the NIR Arm 1. Future gas observations with higher angular resolution are needed to more accurately determine the location of the arm in the gas. Tentatively, we regard the Boehler et al. (2018) result as evidence for ^{13}CO emission originating from a layer close to the disk surface.

4.2.2. Where Is Arm 2 in Submillimeter Emission

Arm 2 is not clearly revealed in our ALMA data. This may be due to less effective trapping of \sim millimeter-sized dust by Arm 2 compared to Arm 1. Specifically, if the two arms are produced by one planet on the outside (the hypothesis raised

by Dong et al. 2015b; see the discussion in Section 4.4), they are expected to have different amplitudes in gas surface density (Figure 5, Fung & Dong 2015; Figure 1, Zhu et al. 2015; Figure 2, Dong et al. 2016a; see also Juhász et al. 2015). This effect probably leads to different dust-trapping capacities, resulting in different arm contrasts, locations, and morphologies in submillimeter continuum emission between the two arms.

Another possibility is that Arm 2 is present but coincides with other features. As shown in Figure 1(d), the south clump and the west part of the inner ring at PA $\sim 220^\circ$ – 320° are located just outside the NIR Arm 2, and the north clump contributes emission at the location of the NIR Arm 2 at PA $\sim 320^\circ$ – 360° . Perhaps some of the emission along a track $\sim 0''.05$ outside the NIR Arm 2 (the red dashed line) comes from an underlying arm structure that cannot be separately identified. Future disk modeling that decomposes the emission in this region to the relevant components are needed to elucidate the situation.

If (1) the MWC 758 disk’s two arms are different in submillimeter continuum emission (e.g., one is present while the other is not) despite their relative symmetry in NIR scattered light and (2) the planet-induced primary and secondary arms do trap dust differently, then a careful comparison between the ALMA observations and the gas+dust simulations of disk–planet interactions may reveal which arm is the primary arm pointing to the hypothetical arm-driving planet. Previous simulations have shown that for multi- M_J planets, the two arms driven by a single planet are nearly equally prominent in scattered light (Dong et al. 2015b, 2016a), making it difficult to break the degeneracy (unless the two arms are found in a near-face-on disk and are not symmetric; Fung & Dong 2015).

Similar to the second interpretation above, the east side of the inner ring at PA $\sim 30^\circ$ – 120° , being slightly outside the NIR Arm 1, may also contain contributions from a north segment of ALMA Arm 1 as the two coincide. In this scenario, the “intrinsic” Arm 1 in submillimeter continuum emission would start all the way north at PA $\sim 30^\circ$, covering a full $\sim 180^\circ$ in the azimuthal direction similar to the NIR Arm 1. The azimuthal asymmetry of the inner ring might be partially induced by the “extra” contributions from the underlying spiral arms.

4.3. Dust Distributions in the Emission Clumps

As both clumps are spatially resolved and marginally optically thin, dust particles contributing to 0.87 mm continuum emission at each clump are distributed in an extended region, with their surface density roughly traced by the surface brightness of the emission. Hydro simulations of dust trapping by $m = 1$ azimuthally asymmetric structures in the gas (e.g., Mittal & Chiang 2015; Baruteau & Zhu 2016; Miranda et al. 2017) generally show effective trapping, resulting in compact dust concentrations if given enough evolution time. Particles of sizes in a finite range, all contributing to submillimeter continuum emission at a single wavelength, can be collected at different azimuthal locations inside one clump, resulting in extended emission over a large azimuthal angle, consistent with our observations (e.g., Mittal & Chiang 2015). In the radial direction, however, particles tend to drift into arcs narrower than the disk scale height, which is usually around 10% of the radius or less. The radial drift timescale depends on the particle size. It is shortest—shorter

than system ages—for particles whose dimensionless stopping times (Stokes numbers St) are on the order of unity.

At the two clumps, the average midplane temperature from the group of representative radiative transfer models introduced in Section 3.4 (26 and 22 K for the south and north clumps, respectively) correspond to a local disk aspect ratio $h/r = 0.059$ (south) and 0.071 (north) (assuming a $1.4M_\odot$ stellar mass; Boehler et al. 2018). The intrinsic radial FWHMs of both clumps in the deprojected image ($FWHM_{\text{intrinsic}}$; Section 3.4) are ~ 4 times the local disk scale height h . Probably the particles traced by the submillimeter emission from the clumps have $St < 1$, as particles with $St \sim 1$ are expected to have drifted to the center of the clumps at the age of the system (smaller particles drift slower in both the radial and azimuthal directions and are more easily diffused by gas turbulence). Also, dust feedback onto gas tends to prevent particles from concentrating toward a single point and is expected when the local dust-to-gas ratio approaches unity (e.g., Fu et al. 2014; Miranda et al. 2017). We also rule out the presence of multiply clustered subclumps separated azimuthally by more than the beam size (6.5 au). Such “multiple clumps” may be produced by dust trapping in vortices generated at a dead-zone edge due to viscosity transitions (Miranda et al. 2017, Figures 6 and 7). Multiple clumps azimuthally separated by less than the beam size are still possible.

If the submillimeter continuum emission is spatially resolved and the dust is optically thin, the azimuthal peak-to-trough ratio at the position of a clump provides an estimate of the underlying contrast in the surface density of \sim millimeter-sized dust. However, since both clumps may only be marginally optically thin at their peaks (Section 3.4), the measured azimuthal contrasts (4.4 for the south and 10 for the north clump) only provide a lower limit on the degree of dust concentration in the clumps.

4.4. The Hypothetical Planets in the MWC 758 Disk

The central cavity of MWC 758 inward of $r \approx 51$ au may be opened by one or more planets inside (e.g., Zhu et al. 2011; Dong et al. 2015c; Duffell & Dong 2015). This cavity, however, has not been revealed in NIR scattered light down to an inner working angle of $\sim 0''.1$ (16 au; Reggiani et al. 2018; cf. Benisty et al. 2015, who reported a slight reduction in scattered-light intensity inside the millimeter-wave cavity). Dong et al. (2012) assigned MWC 758 to the group of transitional disks with “missing cavities.” The data taken collectively are consistent with the gas inside the cavity having been depleted by no more than a factor of 10–100; millimeter-sized particles may be trapped at the overpressured cavity edge, but smaller micron-sized dust can still leak in with the gas (Dong et al. 2012). The ellipticity of the cavity edge and the possibility that the south clump may be a vortex formed at the cavity edge as triggered by the Rossby wave instability (RWI; see below) further constrain the properties of the disk and embedded planets (Section 4.1). Determining the degree of gas depletion inside the cavity using gas emission observations (e.g., van der Marel et al. 2015, 2016) will be essential.

The two spirals may be excited by an ~ 5 – $10 M_J$ planet exterior to the spirals at ~ 100 au, as proposed by Dong et al. (2015b). A more massive companion even further away may also be able to drive the arms (e.g., Dong et al. 2016c) but has been ruled out by observations (Reggiani et al. 2018). Massive, distant planets like the one predicted around MWC 758 have

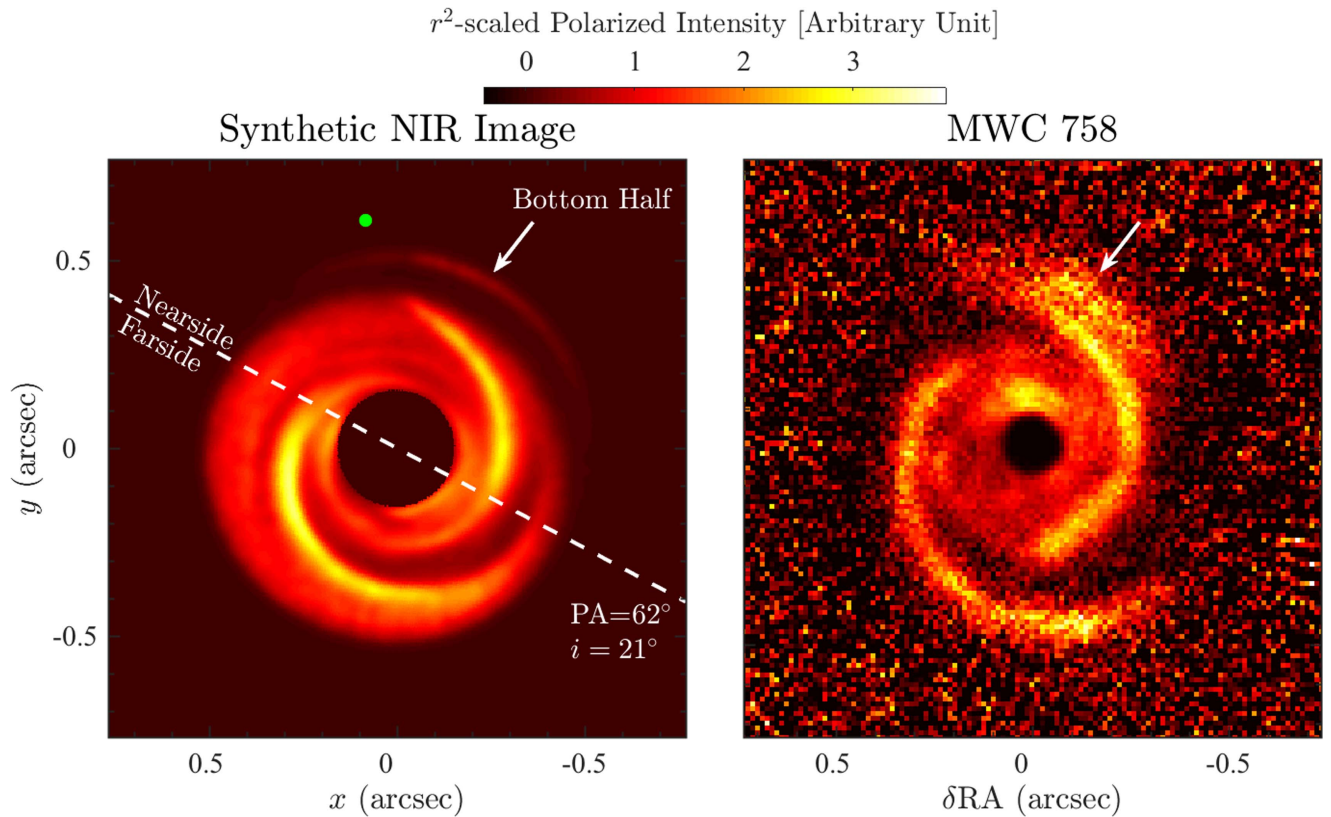


Figure 6. Left: simulated NIR polarized-light image of a disk perturbed by a planet. Right: Y-band ($1\ \mu\text{m}$) polarized-light image of MWC 758 (Benisty et al. 2015). Both the model and the observation have been r^2 -scaled. The simulation is based on Model 6ISO125 in Dong et al. (2015b), in which the planet has $M_p = 6 \times 10^{-3} M_*$ (M_* is the stellar mass) and is located at 100 au. The disk is truncated at 80 au (i.e., roughly at the inner edge of the gap opened by the planet). The synthetic observation is produced using the geometry of MWC 758 (Isella et al. 2010; Boehler et al. 2018): the southeast side is the far side, inclination $i = 21^\circ$, and position angle $PA = 62^\circ$ (major axis marked by the dashed line). The green dot marks the projected location of the planet. If the outer disk is effectively truncated by the planet, the feature next to the northern arm in the actual observation (indicated by the arrow) can be explained as the near-side edge of the bottom (obscured) half of the disk. See Section 4.4 for discussion.

been found around other A-type stars (e.g., HR 8799 b, Marois et al. 2008; see also Bowler 2016; note that MWC 758 will probably become a main-sequence A-type star in the future). The formation of such planets is currently being investigated; they might be the outcomes of GI and disk fragmentation at early times (e.g., Rafikov 2005; Kratter et al. 2010). The new ALMA data are consistent with the Dong et al. (2015b) hypothesis, as the presence of Arm 1 in submillimeter continuum emission suggests that it is mainly an overdensity rather than a shadow or temperature structure. The fact that Arm 2 is not clearly revealed by ALMA may be caused by different dust-trapping capacities in the primary and secondary arms (Section 4.2.2).

A massive (multi- M_J) companion at around 100 au exterior to the arms is also expected to truncate the disk interior to its orbit. Disk truncation is seen not just in scattered light but also in ALMA observations of C^{18}O , revealing an outer gas disk edge at ~ 100 au (Boehler et al. 2018). We note that emission from ^{13}CO , a more abundant species, is detected out to ~ 150 au (Boehler et al. 2018). Future gas emission modeling work is needed to quantify the spatial distribution of gas outside the main submillimeter disk ring. Figure 6 shows a synthetic scattered-light image based on the Dong et al. (2015b) disk model. It is identical to the original one (see Figure 4 in that paper), except (1) the disk at $r \geq 0.8r_p$ (see, e.g., Figure 2 of Fung & Chiang 2016) is removed prior to image synthesizing, and (2) the synthetic image is produced

assuming not the face-on but the actual viewing geometry of the disk: $PA = 62^\circ$, $i = 21^\circ$, and with the northwest side being the side nearest the observer (Isella et al. 2010; Boehler et al. 2018). We note that the 3D hydro simulation has been run for 20 orbits, which is long enough for the spiral arms to be fully established and reach steady state but not enough for the gap around the planet’s orbit to be fully opened. To fully truncate the disk, simulations would need to be run for a much longer time, which is prohibitively expensive in this case. Hence, we truncate the disk manually. Future simulations run to the system age are needed to examine whether the truncation of the disk with the right radius and depletion can be naturally achieved by the planet.

Figure 6 shows that the near-side edge of the bottom half of the disk in the model image (left panel; indicated by the arrow), just outside and parallel to the tip of Arm 2, is clearly visible and in good agreement with the location and orientation of the corresponding structure in the actual SPHERE image (right panel; indicated by the arrow). Note that while non-planet-based mechanisms can also produce a sharp outer edge in the distribution of \sim millimeter-sized dust due to dust radial drift (e.g., Birnstiel & Andrews 2014), the presence of this NIR feature requires a truncation and sharp edge in the distribution of \sim micron-sized small dust, usually well coupled with the gas. Such a structure has also been seen in the Dong et al. (2016a, Figure 5) study of spiral arm morphology in inclined disks and in HD 100453 (Benisty et al. 2017), a disk with a truncated

edge and two spirals. Our model feature is fainter than in the SPHERE image. This may be due to the specific properties of submicron-sized dust in MWC 758 responsible for NIR scattered light (interstellar medium dust is assumed in the model; Kim et al. 1994).

A few direct-imaging campaigns have been carried out to look for this companion, with no confirmed detection at the moment. The achieved detection limit on the planet mass assuming “hot-start” planet formation models, which predict a higher luminosity for a planet of a given mass at a given age than the “warm” or “cold” formation models (Spiegel & Burrows 2012), is approaching the theoretical prediction ($\sim 5M_J$ at $r \sim 100$ au; Reggiani et al. 2018). The implication of such results is far from certain. Possibilities include (1) planets are not as luminous as the hot-start model predictions and (2) the system is older than the often-assumed 3.5 ± 2 Myr (Meeus et al. 2012), making the hypothetical planet colder and less luminous (particularly in hot-start models). Age estimates for pre-main-sequence stars are usually made by placing the stars on the H-R diagram and comparing their locations with theoretical isochrones. Meeus et al. (2012) assumed the old *Hipparcos* distance of 279 pc for MWC 758 (van Leeuwen 2007), which is significantly greater than the new *Gaia* distance of 160 pc, and therefore overestimated its luminosity by a factor of 3. Reexamination of the stellar age using the *Gaia* distance is needed. Similarly, previous stellar-mass (M_*) determinations from isochrone fitting are likely to be inaccurate. Disk kinematic studies can independently and more accurately determine M_* (e.g., Isella et al. 2010; Czekala et al. 2015) and thereby better calibrate the hydrodynamic and radiative transfer simulations of planet–disk interactions that all scale with M_* .

The nondetection of the CPD in our ALMA observations also constrains the CPD models. Wu et al. (2017) searched for but failed to detect millimeter continuum emission from the CPDs around five known planetary-mass companions at large distances in other systems using ALMA (see also the nondetections by Bowler et al. 2015 and MacGregor et al. 2017). The authors proposed that CPDs may be compact, having sizes on the order of 100 Jupiter radii or smaller, and optically thick, under which conditions the \sim millimeter flux density from such a disk is expected to be on the order of a μ Jy, well below our rms noise level. Alternatively, the predicted companion outside the disk edge in MWC 758 may not have a CPD—its CPD may have been lost through accretion, and it is not being replenished by an outer disk beyond the planet’s orbit.

The two azimuthal clumps in \sim millimeter emission have also been proposed to be dust-trapping vortices generated by the RWI at the edges of planet-opened gaps (Lovelace et al. 1999; Li et al. 2000). The north clump has been shown to be more compact at longer wavelengths (Marino et al. 2015), consistent with being an azimuthal dust trap (e.g., Lyra & Lin 2013; Zhu & Stone 2014). Our new data showed that the radial extent (FWHM) of the dust distribution inside the clumps (particularly the north clump) may be $\sim 4 \times$ the local disk scale height, indicating that the dust back-reaction onto the gas may be important (Section 4.3). The proposed spiral-arm-driving planet exterior to the spirals may naturally sharpen the edge of the disk at ~ 100 au, triggering the RWI and, subsequently, the formation of a vortex as the north clump.

Finally, the triple-ring structure best seen on the west side of the broad outer disk may also hint at the presence of planets. Dong et al. (2017a; see also Bae et al. 2017) showed that such a structure may be produced by a single planet in low-viscosity gas. The rich dynamical environment in MWC 758 with possible eccentric-cavity-opening planets inside and a spiral-driving planet outside makes simple model–data comparison difficult. The eccentricity of the observed gaps and rings ($e \approx 0.1$) also adds an additional complication. Object-specific modeling taking into account relevant dynamical processes, including planet–planet interactions, is needed to comment on the origin of these narrow gaps.

4.5. New Questions and Future Work

The new data and analysis motivate future theoretical and observational studies.

1. Gas+dust simulations to study whether and how planet-induced multiple spiral arms can trap dust particles and the difference between the primary and secondary arms.
2. Disk modeling to decompose the emission in the broad ring into components to examine whether unidentified segments of the two arms, particularly Arm 2, are hidden under other, more prominent structures.
3. Combining the above studies to examine which of the two arms is the primary (companion-pointing) arm, should they be excited by a single companion. The outcome can direct future direct-imaging campaigns to search for this companion.
4. Continuum emission observations at multiple submillimeter to centimeter wavelengths and spectral index analysis to examine the composition and size distribution of the dust in the two clumps. Comparing the data with vortex dust-trapping simulations to understand the effect of dust feedback onto the gas.
5. Simulations to explore whether a companion at 100 au or further can excite the two spirals, truncate the disk, and trigger the formation of the north clump at the truncated disk edge simultaneously.

5. Summary









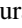
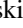
We present Cycle 5 ALMA continuum emission observations of the protoplanetary disk around MWC 758 at 0.87 mm with a beam size of 43×39 mas (6.8×6.2 au) and an rms noise level of $20 \mu\text{Jy beam}^{-1}$. This system joins a few other protoplanetary disks revealed by high-sensitivity ALMA observations with sub- $0''.05$ resolution (HL Tau, ALMA Partnership et al. 2015; Akiyama et al. 2016a; TW Hya, Andrews et al. 2016; Tsukagoshi et al. 2016; Huang et al. 2018; V883, Cieza et al. 2016; and V1247 Orionis, Kraus et al. 2017; see also GY 91, Sheehan & Eisner 2018). The high-resolution submillimeter continuum map (Figure 1) reveals a central cavity $\sim 0''.32$ (51 au) in size, a broad outer disk extending to $\sim 0''.64$ (102 au) that can be decomposed into three faint rings, a south clump on the outer edge of the cavity, a north clump on the outer edge of the outer disk, a central emission point source around the star, and a spiral arm in the south. The basic measurements of the features are listed in Table 1. We compare the ALMA data set with observations at other wavelengths and propose possible interpretations for the observed disk structures. Our main conclusions are as follows:

1. One of the two spiral arms imaged in NIR scattered light (Arm 1 in Figure 1(c)) is revealed in submillimeter continuum emission. This is the first time the submillimeter continuum counterpart of an NIR spiral arm is spatially resolved. The ALMA arm extends about 90° in the azimuthal direction, and $2/3$ of its extent is located at a slightly larger (up to 8%) stellocentric distance than its scattered-light image counterpart. This offset can be explained as the surface (probed by NIR scattered light) and the midplane (probed by submillimeter continuum emission) of the same structure being projected to different locations on the sky (Figures 4 and 5). The azimuthal peak-to-trough contrast of the arm, 3.6, suggests that it is mainly a density (emission optical depth) feature.
2. Contrary to Arm 1, Arm 2 (Figure 1(c)) is not clearly revealed in the ALMA image. We submit two possible explanations: (A) Arm 2 does not trap \sim millimeter-sized dust as effectively as Arm 1 (due to, for example, the difference between the primary and secondary arms' gas perturbation amplitudes, as excited by one planet), making Arm 2 weaker/absent in submillimeter continuum emission; and (B) Arm 2 is present at a slightly larger stellocentric distance coinciding with the east side of the inner ring and the clumps, making it difficult to identify. We favor the former explanation.
3. The cavity (and the inner ring that defines its edge) is not a circle centered on the star. This is not a projection effect. Once deprojected, the inner ring can be fit by an ellipse with eccentricity $e \approx 0.1$ and one focus on the star (Figures 2(c) and (d)). If fit by a circle, its center is at ~ 30 mas from the *Gaia* stellar location, which roughly coincides with the detected central point source. This difference is \sim one order of magnitude larger than the expected ALMA astrometry uncertainty. The middle and outer rings also tentatively show the same eccentricity and orientation as the inner ring. Hydro simulations have shown that companions may open eccentric gaps under certain conditions (e.g., Kley & Dirksen 2006).
4. Both the north ($r_{\text{deprojected}} = 0''.53 = 85$ au) and the south clump ($r_{\text{deprojected}} = 0''.31 = 50$ au) are spatially resolved in the radial and azimuthal directions. Their radial FWHM-to-radius ratios are $\sim 21\%$ (south) and 29% (north), both being $\sim 4\times$ the local disk aspect ratio h/r . Azimuthally, their FWHMs are about $1/6$ of a circle. The two clumps may be only marginally optically thin. Their significant radial widths suggest that emitting particles have Stokes numbers smaller than unity and/or have been smeared out by dust-to-gas back-reaction, as particles with $St \sim 1$ are expected to have drifted to the center of the clumps at the age of the system.
5. The northwest feature parallel to Arm 2 in the NIR imaging observations of the disk can be explained as the near-side edge of the bottom half of the disk, if the disk is truncated at the outer edge of the spiral arms (Figure 6). The disk truncation, the two spiral arms, and the north clump all point toward an unseen external companion at around ~ 100 au.

We are grateful to Hui Li for useful discussions, Myriam Benisty for making available the SPHERE image of MWC 758, and an anonymous referee for constructive suggestions that

largely improved the quality of the paper. Numerical calculations were performed on the SAVIO cluster provided by the Berkeley Research Computing program, supported by the UC Berkeley Vice Chancellor for Research and the Berkeley Center for Integrative Planetary Science. Y.P. was supported by Russian Science Foundation grant 17-12-01168. This paper makes use of the following ALMA data: 2017.1.00492.S. ALMA is a partnership of the ESO (representing its member states), NSF (USA), and NINS (Japan), together with the NRC (Canada), *MOST* and ASIAA (Taiwan), and KASI (Republic of Korea), in cooperation with the Republic of Chile. The Joint ALMA Observatory is operated by the ESO, AUI/NRAO, and NAOJ. The National Radio Astronomy Observatory is a facility of the National Science Foundation operated under cooperative agreement by Associated Universities, Inc. Y.H. is currently supported by the Jet Propulsion Laboratory, California Institute of Technology, under a contract with the National Aeronautics and Space Administration. This work was supported by NAOJ ALMA Scientific Research Grant Number 2016-02A. This research is supported by the Ministry of Science and Technology of Taiwan through grant MOST 106-2119-M-001-013.

ORCID iDs

Ruobing Dong  <https://orcid.org/0000-0001-9290-7846>
 Josh Eisner  <https://orcid.org/0000-0002-1031-4199>
 Sean Andrews  <https://orcid.org/0000-0003-2253-2270>
 Eugene Chiang  <https://orcid.org/0000-0002-6246-2310>
 Simon Casassus  <https://orcid.org/0000-0002-0433-9840>
 Thomas Esposito  <https://orcid.org/0000-0002-0792-3719>
 David Wilner  <https://orcid.org/0000-0003-1526-7587>
 Eiji Akiyama  <https://orcid.org/0000-0002-5082-8880>
 Motohide Tamura  <https://orcid.org/0000-0002-6510-0681>
 John Wisniewski  <https://orcid.org/0000-0001-9209-1808>

References

- Akiyama, E., Hasegawa, Y., Hayashi, M., & Iguchi, S. 2016a, *ApJ*, 818, 158
 Akiyama, E., Hashimoto, J., Liu, H. B., et al. 2016b, *AJ*, 152, 222
 ALMA Partnership, Brogan, C. L., Pérez, L. M., et al. 2015, *ApJL*, 808, L3
 Andrews, S. M., Wilner, D. J., Espaillat, C., et al. 2011, *ApJ*, 732, 42
 Andrews, S. M., Wilner, D. J., Zhu, Z., et al. 2016, *ApJL*, 820, L40
 Arzamas, L., & Rafikov, R. R. 2018, *ApJ*, 854, 84
 Ataiee, S., Pinilla, P., Zsom, A., et al. 2013, *A&A*, 553, L3
 Avenhaus, H., Quanz, S. P., Schmid, H. M., et al. 2017, *AJ*, 154, 33
 Bae, J., & Zhu, Z. 2018a, *ApJ*, 859, 118
 Bae, J., & Zhu, Z. 2018b, *ApJ*, 859, 119
 Bae, J., Zhu, Z., & Hartmann, L. 2016, *ApJ*, 819, 134
 Bae, J., Zhu, Z., & Hartmann, L. 2017, *ApJ*, 850, 201
 Baruteau, C., & Zhu, Z. 2016, *MNRAS*, 458, 3927
 Benisty, M., Juhasz, A., Boccaletti, A., et al. 2015, *A&A*, 578, L6
 Benisty, M., Stolker, T., Pohl, A., et al. 2017, *A&A*, 597, A42
 Birmstiel, T., & Andrews, S. M. 2014, *ApJ*, 780, 153
 Boehler, Y., Ricci, L., Weaver, E., et al. 2018, *ApJ*, 853, 162
 Bowler, B. P. 2016, *PASP*, 128, 102001
 Bowler, B. P., Andrews, S. M., Kraus, A. L., et al. 2015, *ApJL*, 805, L17
 Bryden, G., Chen, X., Lin, D. N. C., Nelson, R. P., & Papaloizou, J. C. B. 1999, *ApJ*, 514, 344
 Canovas, H., Ménard, F., Hales, A., et al. 2013, *A&A*, 556, A123
 Canovas, H., Montesinos, B., Schreiber, M. R., et al. 2018, *A&A*, 610, A13
 Canovas, H., Schreiber, M. R., Cáceres, C., et al. 2015, *ApJ*, 805, 21
 Casassus, S., Marino, S., Lyra, W., et al. 2018, *MNRAS*, submitted (arXiv:1805.03023)
 Christiaens, V., Casassus, S., Perez, S., van der Plas, G., & Ménard, F. 2014, *ApJL*, 785, L12
 Cieza, L. A., Casassus, S., Tobin, J., et al. 2016, *Natur*, 535, 258
 Corder, S., Eisner, J., & Sargent, A. 2005, *ApJL*, 622, L133
 Currie, T., Muto, T., Kudo, T., et al. 2014, *ApJL*, 796, L30
 Czekala, I., Andrews, S. M., Jensen, E. L. N., et al. 2015, *ApJ*, 806, 154

- Debes, J. H., Jang-Condell, H., Weinberger, A. J., Roberge, A., & Schneider, G. 2013, *ApJ*, 771, 45
- Dipierro, G., Pinilla, P., Lodato, G., & Testi, L. 2015, *MNRAS*, 451, 974
- Dipierro, G., Ricci, L., Pérez, L., et al. 2018, *MNRAS*, 475, 5296
- Dong, R., & Fung, J. 2017, *ApJ*, 835, 38
- Dong, R., Fung, J., & Chiang, E. 2016a, *ApJ*, 826, 75
- Dong, R., Hall, C., Rice, K., & Chiang, E. 2015a, *ApJL*, 812, L32
- Dong, R., Li, S., Chiang, E., & Li, H. 2017a, *ApJ*, 843, 127
- Dong, R., Rafikov, R., Zhu, Z., et al. 2012, *ApJ*, 750, 161
- Dong, R., van der Marel, N., Hashimoto, J., et al. 2017b, *ApJ*, 836, 201
- Dong, R., Vorobyov, E., Pavlyuchenkov, Y., Chiang, E., & Liu, H. B. 2016b, *ApJ*, 823, 141
- Dong, R., Zhu, Z., Fung, J., et al. 2016c, *ApJL*, 816, L12
- Dong, R., Zhu, Z., Rafikov, R. R., & Stone, J. M. 2015b, *ApJL*, 809, L5
- Dong, R., Zhu, Z., & Whitney, B. 2015c, *ApJ*, 809, 93
- Draine, B. T. 2006, *ApJ*, 636, 1114
- Duffell, P. C., & Chiang, E. 2015, *ApJ*, 812, 94
- Duffell, P. C., & Dong, R. 2015, *ApJ*, 802, 42
- Dullemond, C. P., & Dominik, C. 2004, *A&A*, 421, 1075
- Dunhill, A. C., Alexander, R. D., & Armitage, P. J. 2013, *MNRAS*, 428, 3072
- Eisner, J. A., Lane, B. F., Hillenbrand, L. A., Akeson, R. L., & Sargent, A. I. 2004, *ApJ*, 613, 1049
- Farris, B. D., Duffell, P., MacFadyen, A. I., & Haiman, Z. 2014, *ApJ*, 783, 134
- Follette, K. B., Rameau, J., Dong, R., et al. 2017, *AJ*, 153, 264
- Fu, W., Li, H., Lubow, S., Li, S., & Liang, E. 2014, *ApJL*, 795, L39
- Fukagawa, M., Tamura, M., Itoh, Y., et al. 2006, *ApJL*, 636, L153
- Fung, J., & Chiang, E. 2016, *ApJ*, 832, 105
- Fung, J., & Dong, R. 2015, *ApJL*, 815, L21
- Fung, J., Shi, J.-M., & Chiang, E. 2014, *ApJ*, 782, 88
- Gaia Collaboration, Brown, A. G. A., Vallenari, A., et al. 2018, *A&A*, in press (arXiv:1804.09365)
- Garufi, A., Quanz, S. P., Avenhaus, H., et al. 2013, *A&A*, 560, A105
- Goldreich, P., & Tremaine, S. 1979, *ApJ*, 233, 857
- Goldreich, P., & Tremaine, S. 1980, *ApJ*, 241, 425
- Goodman, J., & Rafikov, R. R. 2001, *ApJ*, 552, 793
- Grady, C. A., Muto, T., Hashimoto, J., et al. 2013, *ApJ*, 762, 48
- Hall, C., Forgan, D., Rice, K., et al. 2016, *MNRAS*, 458, 306
- Hall, C., Rice, K., Dipierro, G., et al. 2018, *MNRAS*, 477, 1104
- Hammer, M., Kratter, K. M., & Lin, M.-K. 2017, *MNRAS*, 466, 3533
- Hashimoto, J., Tamura, M., Muto, T., et al. 2011, *ApJL*, 729, L17
- Hord, B., Lyra, W., Flock, M., Turner, N. J., & Mac Low, M.-M. 2017, *ApJ*, 849, 164
- Hsieh, H.-F., & Gu, P.-G. 2012, *ApJ*, 760, 119
- Huang, J., Andrews, S. M., Cleeves, L. I., et al. 2018, *ApJ*, 852, 122
- Isella, A., Guidi, G., Testi, L., et al. 2016, *PhRvL*, 117, 251101
- Isella, A., Natta, A., Wilner, D., Carpenter, J. M., & Testi, L. 2010, *ApJ*, 725, 1735
- Isella, A., Tatulli, E., Natta, A., & Testi, L. 2008, *A&A*, 483, L13
- Juhász, A., Benisty, M., Pohl, A., et al. 2015, *MNRAS*, 451, 1147
- Juhász, A., & Rosotti, G. P. 2018, *MNRAS*, 474, L32
- Kalas, P., Graham, J. R., & Clampin, M. 2005, *Natur*, 435, 1067
- Kama, M., Pinilla, P., & Heays, A. N. 2016, *A&A*, 593, L20
- Kim, S.-H., Martin, P. G., & Hendry, P. D. 1994, *ApJ*, 422, 164
- Kley, W., & Dirksen, G. 2006, *A&A*, 447, 369
- Kratter, K., & Lodato, G. 2016, *ARA&A*, 54, 271
- Kratter, K. M., Murray-Clay, R. A., & Youdin, A. N. 2010, *ApJ*, 710, 1375
- Kraus, S., Kreplin, A., Fukagawa, M., et al. 2017, *ApJL*, 848, L11
- Langlois, M., Pohl, A., Lagrange, A.-M., et al. 2018, arXiv:1802.03995
- Lee, E. J., & Chiang, E. 2016, *ApJ*, 817, 90
- Lee, W.-K. 2016, *ApJ*, 832, 166
- Li, H., Finn, J. M., Lovelace, R. V. E., & Colgate, S. A. 2000, *ApJ*, 533, 1023
- Li, J. I., Liu, H. B., Hasegawa, Y., & Hirano, N. 2017, *ApJ*, 840, 72
- Lin, D. N. C., & Papaloizou, J. C. B. 1993, in *Protostars and Planets III*, ed. E. H. Levy & J. I. Lunine (Tucson, AZ: Univ. Arizona Press), 749
- Liu, H. B., Takami, M., Kudo, T., et al. 2016, *SciA*, 2, e1500875
- Liu, H. B., Vorobyov, E. I., Dong, R., et al. 2017, *A&A*, 602, A19
- Long, Z. C., Fernandes, R. B., Sitko, M., et al. 2017, *ApJ*, 838, 62
- Lovelace, R. V. E., Li, H., Colgate, S. A., & Nelson, A. F. 1999, *ApJ*, 513, 805
- Lubow, S. H. 1991a, *ApJ*, 381, 259
- Lubow, S. H. 1991b, *ApJ*, 381, 268
- Lyra, W., & Lin, M.-K. 2013, *ApJ*, 775, 17
- Lyra, W., Richert, A. J. W., Boley, A., et al. 2016, *ApJ*, 817, 102
- MacGregor, M. A., Wilner, D. J., Czekala, I., et al. 2017, *ApJ*, 835, 17
- Maire, A.-L., Stolker, T., Messina, S., et al. 2017, *A&A*, 601, A134
- Marino, S., Casassus, S., Perez, S., et al. 2015, *ApJ*, 813, 76
- Marois, C., Macintosh, B., Barman, T., et al. 2008, *Sci*, 322, 1348
- Martin, R. G., & Lubow, S. H. 2011, *MNRAS*, 413, 1447
- McMullin, J. P., Waters, B., Schiebel, D., Young, W., & Golap, K. 2007, in *ASP Conf. Ser. 376, Astronomical Data Analysis Software and Systems XVI*, ed. R. A. Shaw, F. Hill, & D. J. Bell (San Francisco, CA: ASP), 127
- Meeus, G., Montesinos, B., Mendigutía, I., et al. 2012, *A&A*, 544, A78
- Meru, F., Juhász, A., Ilee, J. D., et al. 2017, *ApJL*, 839, L24
- Miranda, R., Li, H., Li, S., & Jin, S. 2017, *ApJ*, 835, 118
- Mittal, T., & Chiang, E. 2015, *ApJL*, 798, L25
- Montesinos, M., & Cuello, N. 2018, *MNRAS*, 475, L35
- Montesinos, M., Perez, S., Casassus, S., et al. 2016, *ApJL*, 823, L8
- Muto, T., Grady, C. A., Hashimoto, J., et al. 2012, *ApJL*, 748, L22
- Ogilvie, G. I., & Lubow, S. H. 2002, *MNRAS*, 330, 950
- Pérez, L. M., Carpenter, J. M., Andrews, S. M., et al. 2016, *Sci*, 353, 1519
- Pinilla, P., Benisty, M., & Birnstiel, T. 2012, *A&A*, 545, A81
- Pinilla, P., de Boer, J., Benisty, M., et al. 2015, *A&A*, 584, L4
- Pohl, A., Benisty, M., Pinilla, P., et al. 2017, *ApJ*, 850, 52
- Pohl, A., Pinilla, P., Benisty, M., et al. 2015, *MNRAS*, 453, 1768
- Rafikov, R. R. 2002, *ApJ*, 569, 997
- Rafikov, R. R. 2005, *ApJL*, 621, L69
- Rafikov, R. R. 2016, arXiv:1601.03009
- Ragusa, E., Dipierro, G., Lodato, G., Laibe, G., & Price, D. J. 2017, *MNRAS*, 464, 1449
- Reggiani, M., Christiaens, V., Absil, O., et al. 2018, *A&A*, 611, A74
- Reid, M. J., Schneps, M. H., Moran, J. M., et al. 1988, *ApJ*, 330, 809
- Ren, B., Dong, R., Esposito, T. M., et al. 2018, *ApJ*, 857, 9
- Rice, W. K. M., Lodato, G., Pringle, J. E., Armitage, P. J., & Bonnell, I. A. 2004, *MNRAS*, 355, 543
- Sheehan, P., & Eisner, J. 2018, *ApJ*, 857, 18
- Spiegel, D. S., & Burrows, A. 2012, *ApJ*, 745, 174
- Stolker, T., Dominik, C., Avenhaus, H., et al. 2016a, *A&A*, 595, A113
- Stolker, T., Dominik, C., Min, M., et al. 2016b, *A&A*, 596, A70
- Stolker, T., Sitko, M., Lazareff, B., et al. 2017, *ApJ*, 849, 143
- Szulágyi, J., van der Plas, G., Meyer, M. R., et al. 2017, *MNRAS*, in press (arXiv:1709.04438)
- Tang, Y.-W., Guilloteau, S., Dutrey, A., et al. 2017, *ApJ*, 840, 32
- Teyssandier, J., & Ogilvie, G. I. 2017, *MNRAS*, 467, 4577
- Tobin, J. J., Kratter, K. M., Persson, M. V., et al. 2016, *Natur*, 538, 483
- Tomida, K., Machida, M. N., Hosokawa, T., Sakurai, Y., & Lin, C. H. 2017, *ApJL*, 835, L11
- Tsukagoshi, T., Nomura, H., Muto, T., et al. 2016, *ApJL*, 829, L35
- Uyama, T., Hashimoto, J., Muto, T., et al. 2018, *AJ*, in press (arXiv:1804.05934)
- van der Marel, N., van Dishoeck, E. F., Bruderer, S., et al. 2016, *A&A*, 585, A58
- van der Marel, N., van Dishoeck, E. F., Bruderer, S., Pérez, L., & Isella, A. 2015, *A&A*, 579, A106
- van Leeuwen, F. 2007, *A&A*, 474, 653
- Wagner, K., Apai, D., Kasper, M., & Robberto, M. 2015, *ApJL*, 813, L2
- Wagner, K., Dong, R., Sheehan, P., et al. 2018, *ApJ*, 854, 130
- Whitney, B. A., Robitaille, T. P., Bjorkman, J. E., et al. 2013, *ApJS*, 207, 30
- Wright, M. C. H., Carlstrom, J. E., Plambeck, R. L., & Welch, W. J. 1990, *AJ*, 99, 1299
- Wu, Y.-L., Close, L. M., Eisner, J. A., & Sheehan, P. D. 2017, *AJ*, 154, 234
- Zhu, Z., Dong, R., Stone, J. M., & Rafikov, R. R. 2015, *ApJ*, 813, 88
- Zhu, Z., Nelson, R. P., Dong, R., Espaillat, C., & Hartmann, L. 2012, *ApJ*, 755, 6
- Zhu, Z., Nelson, R. P., Hartmann, L., Espaillat, C., & Calvet, N. 2011, *ApJ*, 729, 47
- Zhu, Z., & Stone, J. M. 2014, *ApJ*, 795, 53